JOURNAL OF MATERIALS SCIENCE 26 (1991) 2157–2168

Fracture mechanics model for subthreshold indentation flaws:

Part I *Equilibrium fracture*

SRINIVASARAO LATHABAI*, J. RÖDEL*, T. DABBS‡, B. R. LAWN
Ceramics Division, National Institute of Standards and Technology, Gaithersburg, MD 20899, USA

A fracture mechanics model for subthreshold indentation flaws is described. The model describes the initiation and extension of a microcrack from a discrete deformation-induced shear "fault" (shear crack) within the contact zone. A stress-intensity factor analysis for the microcrack extension in residual-contact and applied-stress fields is used in conjunction with appropriate fracture conditions, equilibrium in Part I and non-equilibrium in Part II, to determine critical instability configurations.

In Part I, the *K*-field relations are used in conjunction with the Griffith requirements for crack equilibrium in essentially inert environments to determine: (i) the critical indentation size (or load) for spontaneous radial crack pop-in from a critical shear fault under the action of residual stresses alone; (ii) the inert strengths of surfaces with subthreshold or postthreshold flaws. The theory is fitted to literature data for silicate glasses. These fits are used to "calibrate" dimensionless parameters in the fracture mechanics expressions, for later use in Part II. The universality of the analysis in its facility to predict the main features of crack initiation and propagation in residual and applied fields will be demonstrated. Special emphasis is placed on the capacity to account for the significant increase in strength (and associated scatter) observed on passing from the postthreshold to the subthreshold domain.

1. Introduction

Crack initiation is an important issue in achieving ultra-high strengths in highly brittle solids, e.g. pristine optical glass fibres in telecommunications applications and crystalline whiskers in ceramics composites. The micromechanics of initiation are believed to hold the key to an understanding of the strength degradation suffered by such pristine surfaces in contact damage, e.g. in impact with dust particles [1, 2]. One of the most powerful methodologies in the study of contact damage is that of indentation fracture. This approach determines a well defined *threshold* in the damage response [3–9]: in postthreshold damage radial cracks extend a distance of an indentation half-diagonal or more from the contact damage zone; in subthreshold damage no such cracks are evident outside the plastic impression. Subthreshold indentations have been used to special advantage as controlled flaws in the evaluation of ultra-high strength properties of brittle materials, notably silicate glasses, under both inert and environmentally interactive conditions [3, 4, 6, 8, 9]. However, whereas the micromechanics of crack initiation have been unequivocally identified [5, 7, 10–12] and effectively modelled in terms of a "pop-in" instability [13–16], the subthreshold-strength studies to date have been largely limited to empirical treatments.

In this paper we present a detailed model that allows for quantitative predictions of subthreshold flaw responses in residual and applied stress fields. The essence of our model is the initiation and extension of a microcrack from a deformation-induced crack nucleus, specifically a "shear fault", within the irreversible contact zone [5, 7, 10, 11]. Such deformation zones may be taken as generically representative of naturally occurring flaws, such as the impact damage sites already mentioned, internal inclusions, surface steps, etc. Our analysis builds on a first attempt at modelling the mechanics of stress-induced crack initiation and subsequent propagation described elsewhere [17]. It recognizes the discreteness of the shear fault as an essential element of stress concentration within the deformation zone, but retains the simplicity of conventional continuum cavity descriptions [18] for determining the crack extension from this fault. The model is universal in that it determines the evolution of fracture at all stages, initiation and propagation, under specified external stress and environment conditions. A pertinent feature is its self-consistency with earlier descriptions of indentation fracture in

---

* *Permanent address*: On leave from the Department of Materials Science and Engineering, Lehigh University, Bethlehem, PA 18015, USA.
‡ *Present address*: CSIRO, Division of Wool Technology, Sydney, NSW 2112, Australia.

0022–2461/91 $03.00 + .12

small- and large-crack limits: in the near residual contact field, with the threshold conditions for spontaneous crack initiation [13–15]; in the far field, with the familiar K-field response for propagating postthreshold cracks in the residual contact field [19, 20] and the strength characteristics for surfaces with postthreshold flaws [9, 21, 22].

Our model will be presented in two parts. In Part I we derive fracture mechanics relations for essentially equilibrium conditions, as pertain to vacuum conditions or non-interactive environments. The issues addressed are: the threshold indentation size and load for crack pop-in; and the inert strength in both the subthreshold and postthreshold domains. We fit the K-field relations to experimental data from the literature for selected silica glasses, including so-called "normal" and "anomalous" glasses [23], and use these fits to adjust configurational, dimensionless shear-fault–microcrack parameters for each of these glasses. In Part II we use these "calibrated" K-field relations in conjunction with independently measured crack velocity functions to predetermine the analogous crack initiation and strength (fatigue) properties in chemically interactive environments. The model will be shown to possess the essential ingredients for a quantitative explanation of distinctly higher strengths in the subthreshold (i.e. relative to the postthreshold) region; and, by varying the location of the nucleating shear fault within the contact near field, associated increases in the scatter.

2. Subthreshold elastic–plastic identation damage in ceramics: background

2.1. Experimental observations

Earlier indentation studies on silicate glasses have been instrumental in revealing the nature of the irreversible deformation beneath sharp point contacts [5–7, 10, 11, 24]. Representative micrographs of subthreshold indentations in soda-lime and fused silica glasses are shown in Fig. 1. Soda-lime is a "normal" glass, in which the deformation is volume conserving; fused silica is "anomalous", with a strong component of densification [23]. Despite some obvious differences in the "plastic" deformation patterns, the two glasses show essentially the same tendency to radial cracking from shear faults at or near the indentation diagonal. Other cracks, e.g. median [25], lateral [26] and cone [23] may also be initiated, but are not of primary importance in the context of strength degradation. We note the conspicuously inhomogeneous nature of the shear fault patterns within the deformation zone, characteristic spacing ≈ 1 µm in soda-lime, somewhat larger in fused silica. The more pronounced shear faults accommodate the bulk of the volume-conserving component of the indentation deformation, via failure of the glass structure at or close to the cohesive strength [5, 7, 10, 11].

The shear faults are the sources of stress concentration from which the strength-degrading radial cracks initiate. Etching brings out the shear fault pattern more clearly, as seen in Fig. 2. It is evident that the faults are somewhat "weak" interfaces, susceptible to penetration by environmental species, and thus have a certain crack-like quality. On the other hand, there must exist substantial frictional shear stresses at these interfaces, for otherwise the surface depression would recover upon removal of the indenter.

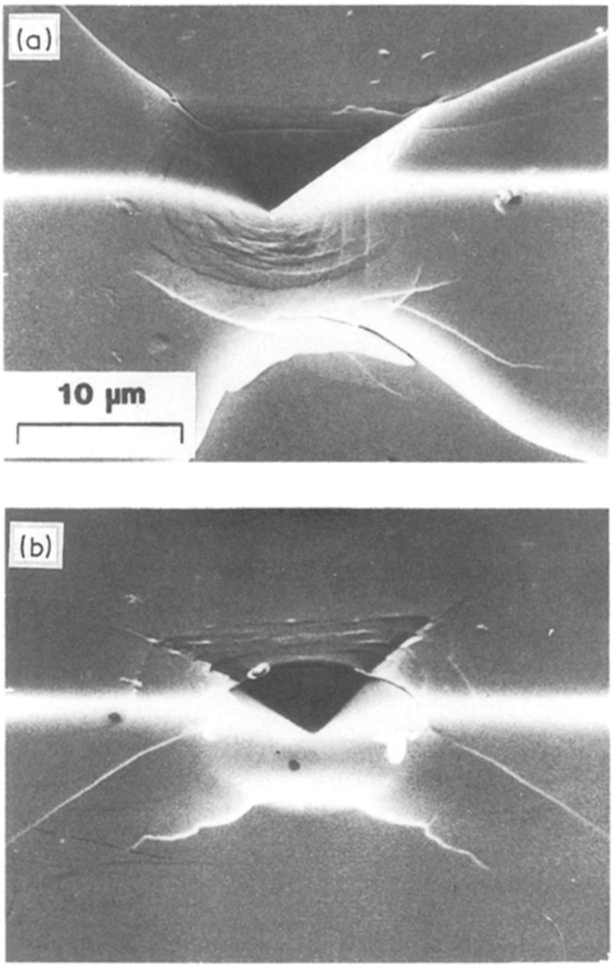

Figure 1 Vickers indentations in (a) soda-lime and (b) fused silica glass, formed at load 2 N, showing shear faults within the contact deformation zone and radial crack extension from these faults near the indentation corners. Scanning electron micrographs, showing half-surface and section views. Note difference in deformation zones below contact. After [7].

The residual contact stresses that are typical of highly brittle solids [19, 20] are due at least in part to this irreversibility. These stresses are especially strong in solids with "normal" deformation behaviour. An important consequence of the residual stress field is the continued evolution of the radial cracks during the unloading stages of indentation [20], although in certain circumstances, e.g. high load [25] or in prolonged contact in the presence of moisture [7] they may pop-in before completion of the indentation loading cycle. Note in Fig. 2b that these same residual stresses, in concert with chemical driving forces from the etching process [27], have induced subsidiary, *post-indentation* radial crack pop-in from the impression corners. The critical conditions for radial crack initiation have been studied in some detail [13–15, 28]. There is a distinctive contact size or load below which pop-in does not occur. This critical size shows pronounced scatter, and is reduced dramatically in the presence of interactive environments

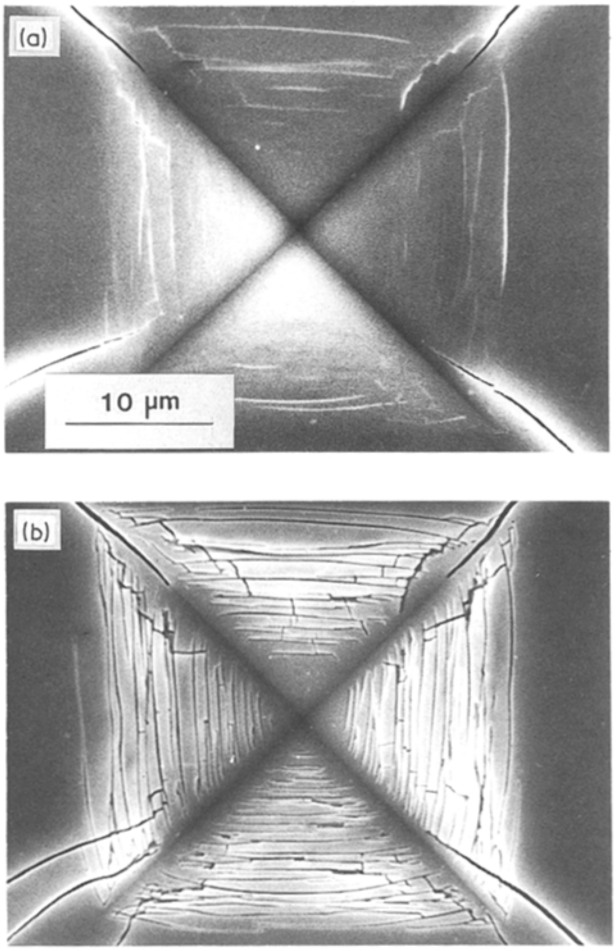

Figure 2 Scanning electron micrographs of Vickers indentations in soda-lime glass, at load 4 N, (a) before and (b) after etching with hydrofluoric acid. Note radial cracks at indentation corners. After [6].

[5, 7]. *Delayed* pop-in can also occur under the latter conditions at relatively low contact sizes, again in those solids with strong residual stress-field intensity. Once the crack has popped in, it can continue to grow stably, either in equilibrium under the action of an applied stress in inert environments or kinetically in reactive environments [19, 21].

Perhaps most significantly, the strength of specimens with subthreshold indentation flaws is significantly higher, and the associated scatter appreciably greater, than one would predict by extrapolation of postthreshold strength data, reflecting a profound difference between the mechanics of initiation- and propagation-controlled failure [3, 8, 22].

2.2. Theoretical descriptions

Theoretical understanding of radial crack evolution relies on detailed knowledge of contact stress fields, particularly the *residual* components of these fields [20, 29]. The problem is comparatively straightforward once the cracks have popped in and entered the far field. In that limit the crack propagation becomes insensitive to configurational details within the contact deformation zone, and the stress-intensity factor associated with the residual tensile stress field may be approximated by a classical central point-force solution for stable penny-like cracks, $K_R \propto P/c^{3/2}$, where c is the crack size and P the indentation load [19]. The residual stress-intensity factor is not fully manifest until an elastic, compressive component in the field is released during withdrawal of the indenter from the surface [20]; hence the above-mentioned observation that pop-in tends to occur toward the end of the contact cycle. With this residual K-field solution, the postthreshold strength properties in subsequent applied tensile loading, under both inert [21] and interactive [30–32] environmental conditions, are readily analysed.

Corresponding stress-intensity factors for the near field are far more complex. Fine details of the contact deformation configuration become crucial elements in the fracture mechanics. In particular, the nature of the nucleation centre within the deformation zone and the attendant local residual stresses determine the critical condition for radial crack pop-in. The first attempt to describe the initiation micromechanics [13] considered the residual stresses in terms of a simplistic, continuous elastic–plastic mismatch stress field at the boundary of the hardness impression. Initiation was assumed to occur from a pre-existent flaw in this field. It was pointed out that for geometrically similar indenters, such as the Vickers pyramid, the intensity of the residual field is load invariant (governed by the hardness), but that the stress-intensity for unstable crack extension from the flaw scales with the indentation size. A critical stress-intensity factor is thereby achieved at a critical indentation load; thence the threshold.

More general stress-intensity factor descriptions that combine the near-field initiation and far-field propagation have since been attempted [15, 16]. These descriptions recognize the extreme complexity of the intermediate residual stress field. However, they make no attempt to incorporate the discreteness of the essential shear fault nucleus described in Section. 2.1, and accordingly lack the basis for a detailed micromechanical description. As mentioned in Section 1, the present study is an elaboration of an earlier preliminary attempt [17] to redress this shortcoming.

We now develop the theme of shear-fault initiation more fully.

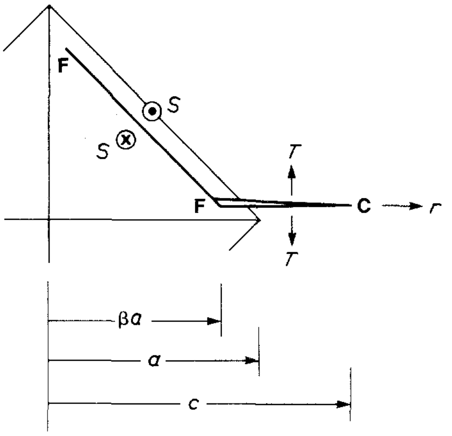

Figure 3 Coordinate system for shear-fault–microcrack model, Vickers indentation. Fault F–F, subjected to shear field (S), develops radial microcrack F–C in tensile field (T).

3. Fracture mechanics model for subthreshold indentation cracks

In this section we present a K-field analysis of the Vickers-indentation shear-fault–microcrack system shown in Fig. 3. We begin by deriving $K(c)$ relations for the system with residual-contact and externally applied stresses. In accordance with the requirements of equilibrium fracture, we then invoke the Griffith plane-strain extension condition $K(c) = K_C = T_0 = [W_0 E/(1 - \nu^2)]^{1/2}$ to determine the critical pop-in conditions and inert strength characteristics: T_0 is the Barenblatt "modulus of cohesion"*; W_0 the Dupré work of adhesion in vacuum (equal to $2\gamma_B$, i.e. twice the intrinsic surface energy of the cracked body), E the elastic modulus and ν Poisson's ratio. In evaluating the equilibria it is necessary to distinguish between stable ($\mathrm{d}K/\mathrm{d}c < 0$) and unstable ($\mathrm{d}K/\mathrm{d}c > 0$) configurations [34].

3.1. Shear-fault–microcrack system

In accordance with our considerations in Section. 2, we assume that a radial crack initiates from the edge of a favourably constrained shear fault near the indentation surface diagonal, as sketched in Fig. 3. The critical fault lies within the contact deformation impression, and is subject to strong compressive and frictional shear tractions which prevent full restoration of the original surface upon indenter removal. It is an interface of weakness in the material (recall the penetrating effect of the etchant in Fig. 2b), and as such may be regarded as having the quality of a shear *crack*.

We first establish a convenient coordinate system. The indentation has a half-diagonal length a, and the crack a length c, measured from the impression centre. For Vickers indentations a is related to the indentation load P by the hardness (defined here relative to projected, not actual, contact area)

$$H = P/2a^2 \qquad (1)$$

The shear fault edge is located within the impression by the intersection distance βa along the half-diagonal; β is a dimensionless quantity which allows us to vary the origin of microcrack extension relative to the impression corner, i.e. $\Delta c = c - \beta a$. In truth, the shear fault has an extremely complicated geometry, curved and inclined downward and inward toward the base of the subsurface deformation zone. In the interest of analytical simplicity we assume it to have a planar half-penny geometry, with surface diameter parallel to impression edge and bounded by impression diagonals as depicted in Fig. 3.

A key factor in radial crack pop-in is the post-indentation residual stress field. This field is sketched as a function of r in Fig. 4, where r is the crack radius measured from the indentation centre. (In measuring r we ignore the angular kink at $c = \beta a$ as the shear fault deflects into the radial crack.) The stress field is separated into two components. Frictional shear stresses are assumed to act radially and uniformly over the area of the initially constrained shear fault S (Fig. 5a)

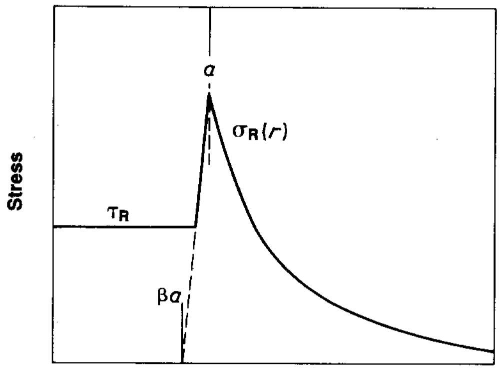

Figure 4 Residual stress distribution for microcrack extension from shear fault at location β: within shear fault interface S, stress τ_R constant (see Fig. 5a); along radial crack plane T, stress σ_R initially rising then subsequently diminishing from expanding cavity field.

$$\tau(r) = \tau_R = \text{constant} \quad (0 \leqslant r \leqslant \beta a) \qquad (2a)$$

$$\tau(r) = 0, \quad (\beta a < r) \qquad (2b)$$

According to the expanding cavity models [18] substantial compressive stresses within the plastic deformation zone act across the fault planes; these do not contribute directly to the (mode II) K-field, and are therefore ignored in our analysis. Outside the deformation zone, however, the same models indicate the presence of *tensile* hoop stresses, which can make a significant contribution to the (mode I) K-field of the radially extending microcrack T. The hoop stresses remain tensile within the radial region $\beta \geqslant \exp(-1/6) = 0.846$ [18]

$$\begin{aligned}\sigma(r) &= \sigma_R[1 - 6\ln(a/r)] \\ &\simeq \sigma_R\{1 - 6[(1 - r/a) + (1 - r/a)^2/2]\}, \\ &\qquad (\beta a \leqslant r \leqslant a) \qquad (3a)\end{aligned}$$

$$\sigma(r) = \sigma_R(a/r)^3, \quad (a \leqslant r) \qquad (3b)$$

where σ_R is the peak value at $r = a$. Again, at $\beta < 0.846$ the hoop stress $\sigma(r)$ becomes compressive; the fault edge then experiences no tension and is therefore unfavourably disposed to radial extension. This restriction locates the viable faults within the range $0.846 \leqslant \beta \leqslant 1$. Strictly, Equation 3 holds only for cavities in *infinite* bodies: free-surface effects should be considered [16]. These effects may, however, be conveniently incorporated into theoretically undetermined numerical factors, which we shall regard as empirically adjustable.

---

*The Barenblatt modulus of cohesion is a material constant

$$T_0 = (2/\pi)^{1/2}\int_0^{\lambda_C} p(\xi)\mathrm{d}\xi/\xi^{1/2} \quad (\lambda_C \ll c)$$

where $p(\xi)$ is the intrinsic interplanar closure stress over the cohesion zone $0 < \xi \leqslant \lambda_C$, and ξ is a crack-plane coordinate measured back from the crack tip [33].

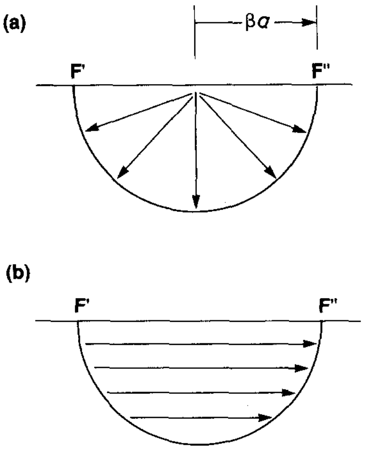

Figure 5 Shear stress distribution over fault plane, (a) from residual frictional stresses in contact field and (b) from subsequently applied tensile stresses normal to radial crack plane. Shear stresses reinforce at edge F″, from which the tensile microcrack ultimately extends.

Note again that Equations 2 and 3 refer to *post*-indentation residual stresses: we indicated in Section 2.2 that the stress field during actual contact contains an additional, reversible, compressive component. Such a component may be simplistically thought of as suppressing the in-contact driving force for crack growth. This will become an especially important consideration when we deal with kinetics in Part II.

For indenters of fixed profile, e.g. Vickers pyramid, the intensity of the stress field is governed uniquely by the hardness defined in Equation 1, i.e. $\tau_R \propto H$, $\sigma_R \propto H$, and is thereby contact-size invariant (geometrical similarity) [13, 15].

3.2. Residual *K*-field and critical pop-in conditions

Now we integrate the residual stresses over the crack area using Green's function formulations for penny-like cracks to obtain a post-indentation stress-intensity function, $K_R(c)$. These integrated functions are available from literature sources. There are two components, the first from the shear stresses in Equation 2 and the second from the tensile stresses in Equation 3.

(i) *Shear component*, K_R^{II}. The radially symmetrical uniform stress τ_R in Fig. 5a makes a mode II contribution to the *K*-field at the surface intersection points F in Fig. 3. For subsequent microcrack extension along the radial direction we have [35]

$$K_R^{II}(c, a, \beta) = \psi_R^S \tau_R c^{1/2}\{\sin^{-1}(\beta a/c) - (\beta a/c)[1 - (\beta a/c)^2]\}, \quad (c \geqslant \beta a) \qquad (4)$$

with ψ_R^S a dimensionless geometrical factor. Note at $c \geqslant \beta a$ that $K_R^{II}(c) \propto c^{-5/2}$, i.e. a short-range contribution.

(ii) *Tensile component*, K_R^I. The tensile stress field makes a mode I contribution, calculable from the standard integral [35]

$$K_R^I(c, a, \beta) = (\psi_R^T/c^{1/2}) \int_{\beta a}^{c} r\sigma(r)\mathrm{d}r/(c^2 - r^2)^{1/2}, \quad (c \geqslant \beta a) \qquad (5)$$

with ψ_R^T another dimensionless factor. This integral may be subdivided into two parts, according to whether the crack extends within the domain of Equations 3a or 3b

$$K_R^I(c, a, \beta) = \psi_R^T \sigma_R c^{1/2}\{6(c/a)[\pi/2 - \sin^{-1}(\beta a/c)] - [1 - (\beta a/c)^2]^{1/2}(8 + 2c^2/a^2 - 6\beta + \beta^2)\}, \quad (\beta a \leqslant c \leqslant a) \qquad (6a)$$

$$K_R^I(c, a, \beta) = \psi_R^T \sigma_R c^{1/2}\{(a/c)^2(1 - a^2/c^2)^{1/2} + 6(c/a)[\sin^{-1}(a/c) - \sin^{-1}(\beta a/c)] + (1 - a^2/c^2)^{1/2}(3 + 2c^2/a^2) - [1 - (\beta a/c)^2]^{1/2}(8 + 2c^2/a^2 - 6\beta + \beta^2)\}, \quad (a \leqslant c) \qquad (6b)$$

At $c \geqslant a$, $K_R^I(c) \rightarrow \psi_R^T \sigma_R a^2/c^{3/2}$, which is the conventional limiting crack-size dependence for centre-loaded indentation cracks [19, 20].

These lengthy expressions may be reduced by making use of the geometrical similarity of the residual stress field intensity mentioned in Section. 3.1 above. Accordingly, we define the dimensionless coefficients*

$$\alpha_R^S = \psi_R^S \tau_R/H = \text{constant} \qquad (7a)$$

$$\alpha_R^T = \psi_R^T \sigma_R/H = \text{constant} \qquad (7b)$$

In the same spirit, we define the separable crack-size function

$$f_R^S(c/a, \beta) = 2(c/a)^{1/2}\{\sin^{-1}(\beta a/c) - (\beta a/c)[1 - (\beta a/c)^2]\}, \quad (c \geqslant \beta a) \qquad (8)$$

for the shear component of the field, and likewise

$$f_R^T(c/a, \beta) = (c/a)^{1/2}\{6(c/a)[\pi/2 - \sin^{-1}(\beta a/c)] - [1 - (\beta a/c)^2]^{1/2}(8 + 2c^2/a^2 - 6\beta + \beta^2)\}, \quad (\beta a \leqslant c \leqslant a) \qquad (9a)$$

$$f_R^T(c/a, \beta) = (c/a)^{1/2}\{(a/c)^2(1 - a^2/c^2)^{1/2} + 6(c/a)[\sin^{-1}(a/c) - \sin^{-1}(\beta a/c)] + (1 - a^2/c^2)^{1/2}(3 + 2c^2/a^2) - [1 - (\beta a/c)^2]^{1/2}(8 + 2c^2/a^2 - 6\beta + \beta^2)\}, \quad (a \leqslant c) \qquad (9b)$$

for the tensile component. The crack-size functions $f_R^S(c/a)$ and $f_R^T(c/a)$ in Equations 8 and 9 are plotted in Fig. 6 for the mean value $\beta = 0.923$ within the allowable range $0.846 \leqslant \beta \leqslant 1$.

Then from the additive property of mechanical-energy-release rates ($G \propto K^2$) for different modes

---

* The limiting condition for Equation 6b at $c \geqslant a$ may be combined with Equations 1 and 7b to obtain $K_R^I(c) = \psi_R^T \sigma_R a^2/c^{3/2} = \alpha_R^T P/2c^{3/2}$. This result is of the same form as traditionally used in indentation fracture [19, 20], $K_R = \chi P/c^{3/2}$, whence we identify $\chi = \alpha_R^T/2$.

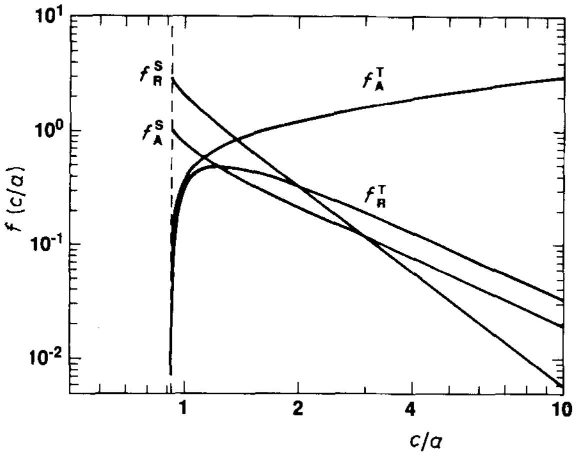

Figure 6 Plot of crack-size weighting functions in Equations 8, 9, 15 and 16, for $\beta = 0.923$.

[36], we may write the net residual stress-intensity factor

$$
\begin{aligned}
K_R(c, a, \beta) &= [(K_R^I)^2 + (K_R^{II})^2]^{1/2} \\
&= Ha^{1/2}\{[\alpha_R^T f_R^T(c/a, \beta)]^2 \\
&\quad + [\alpha_R^S f_R^S(c/a, \beta)]^2\}^{1/2} \qquad (10)
\end{aligned}
$$

The indentation–load dependence now enters solely through the multiplicative factor $a^{1/2}$. Normalized plots of $K_R(c/a)/Ha^{*1/2}$ at fixed β are given in Fig. 7 for indentation sizes $a_1 < a_2 < a_3 < a_4$ (with a^* the critical indentation size for initiation, see below). There are two principal branches, labelled 1 and 2 in the plot, with equilibria at c_1 and c_2: the first with $\mathrm{d}K_R(c)/\mathrm{d}c > 0$ is an unstable branch; the second with $\mathrm{d}K_R(c)/\mathrm{d}c < 0$ is stable; a subsidiary branch labelled 0 is to the left of the secondary minimum at $c = c_I < a$.

We emphasize once more that the formulation culminating in Equation 10 pertains to the *residual* field. Recall from Sections 2.2 and 3.1 that the crack driving forces during indentation are suppressed by an elastic compressive component, in which case we may tentatively take $K_R = 0$ up to the point of indenter removal. We shall need to re-examine this premise when we consider the possibility of chemically assisted in-contact crack initiation in Part II.

The configuration for *spontaneous, post-indentation pop-in* is represented by curve a_3 in Fig. 7. The minimum at c_I on this curve satisfies the condition for unstable equilibrium, i.e. $K_R(c_I^*/a^*) = K_C = T_0$ (horizontal broken line), $\mathrm{d}^2K/\mathrm{d}c^2 > 0$, where the asterisk denotes the critical point. Inserting this requirement in Equation 10 and invoking Equation 1, we obtain

$$a^* = \Theta(T_0/H)^2 \qquad (11a)$$

$$P^* = 2\Theta T_0^4/H^3 \qquad (11b)$$

where $\Theta = 1/\{[\alpha_R^T f_R^T(c_I^*/a, \beta)]^2 + [\alpha_R^S f_R^S(c_I^*/a, \beta)]^2\} =$ constant. This is the result derived in an earlier theory of crack initiation [13]. We may deduce from Fig. 6 that $f_R^T(c_I^*/a) \ll f_R^S(c_I^*/a)$, i.e. the critical condition is dominated by the shear-fault component of the residual stress field. At $K_R(c_2^*/a^*) = T_0$ the crack arrests at stable branch 2.

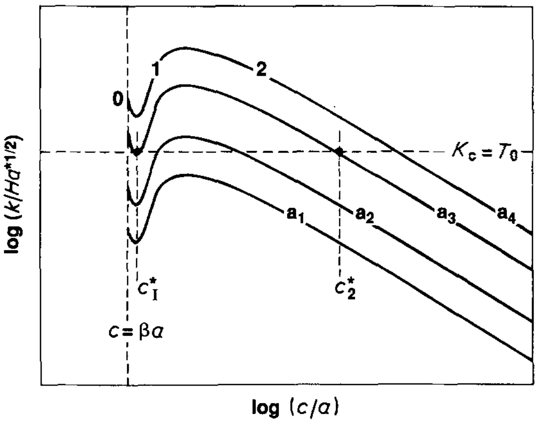

Figure 7 Variation of residual normalized stress-intensity factor with normalized crack size, for fixed β. Branches 0 and 2 are stable, branch 1 unstable. Equilibrium crack length (satisfying $K = K_C = T_0$) occur at c_0 and c_1 (not shown), c_2. Note minimum at c_I ($c_0 \leqslant c_I \leqslant c_1$). The asterisk denotes critical configuration. Curves represent indentation sizes: a_1, subthreshold (zero potential for pop-in); a_2, subthreshold (potential for subcritical pop-in – see Part II); $a_3 = a^*$, threshold; a_4, postthreshold.

3.3. Applied stress and inert strength

Consider now the response of an equilibrium (environment-free) indentation flaw system to an externally applied tensile stress, σ_A. For simplicity we suppose the applied stress to act normal to the radial crack plane. Let us determine the "failure" conditions for the indentation flaw to become unconditionally unstable.

As in the previous subsection, there are two contributions to the applied stress-intensity factor, one from resolved shear stresses acting on the deformation-fault plane and the other from the tensile stress acting directly on the radial-crack plane.

(i) *Shear component*, K_A^{II}. The resolved shear stresses $\tau_A (\propto \sigma_A)$ act uniformly but *parallel* to the specimen surface, reinforcing the residual shear stresses at the tensile corner, Fig. 5b. This makes another mode II contribution to the K-field at the specimen surface [35, 37]*

$$
\begin{aligned}
K_A^{II}(c, a, \beta) &= \psi_A^S \tau_A c^{1/2}\{[1 - (1 - (\beta a/c)^2)^{1/2}] \\
&\quad - [\nu/(2 - \nu)][1 - (1 - (\beta a/c)^2)^{3/2}]\} \\
&\quad (c \geqslant \beta a) \qquad (12)
\end{aligned}
$$

(ii) *Tensile component*, K_A^I. The applied tension manifests itself as a mode I component, again calculable from the standard integral [35]

$$
\begin{aligned}
K_A^I(c, a, \beta) &= (\psi_A^T/c^{1/2}) \int_{\beta a}^{c} r\sigma_A \mathrm{d}r/(c^2 - r^2)^{1/2} \\
&= \psi_A^T \sigma_A c^{1/2}[1 - (\beta a/c)^2]^{1/2}, \quad (c \geqslant \beta a) \qquad (13)
\end{aligned}
$$

Note that at $c \gg a$, $K_A^I(c, a, \beta) \rightarrow \psi_A^T \sigma_A c^{1/2}$, i.e. independent of a or β, which is the familiar result for cracks in uniform tensile fields [36].

We may reduce the expressions by defining the dimensionless coefficients

$$\alpha_A^S = \psi_A^S \tau_I^0/H = \text{constant} \qquad (14a)$$

$$\alpha_A^T = \psi_A^T \sigma_I^0/H = \text{constant} \qquad (14b)$$

---

[*] And a mode III *below* the surface, neglected here because the net shear component of the K-field is maximum at point F″ in Fig. 5a and b.

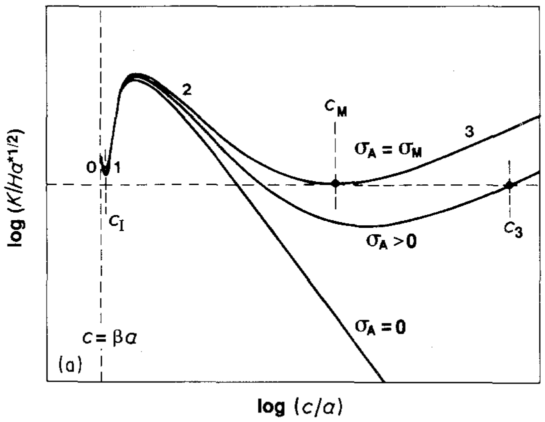

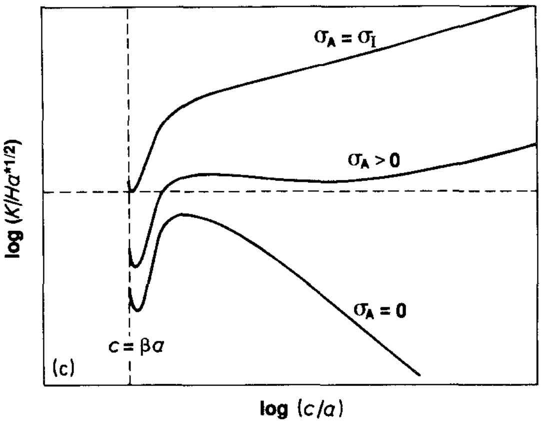

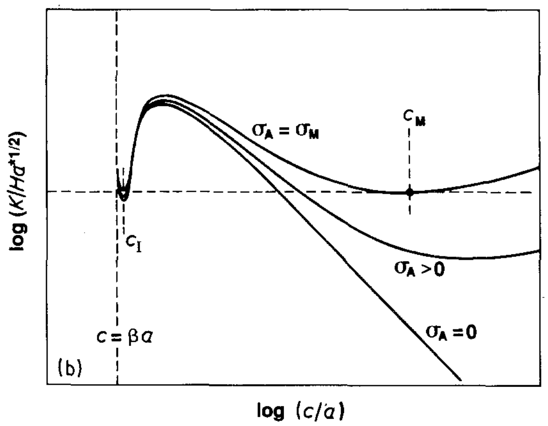

Figure 8 Variation of total stress-intensity factor with crack size, for fixed β. Branches 0 and 2 are stable, 1 and 3 unstable. Equilibrium crack lengths c_M and c_3 at $K = K_C = T_0$ indicated (other equilibrium lengths at c_0, c_I, c_1 and c_2 not shown). Plots illustrate different strength regions: (a) postthreshold, (b) subthreshold with activated failure, and (c) subthreshold with spontaneous failure. Each diagram shows curves for three fixed applied stress levels.

in analogy to Equation 7, where σ_I^0 and τ_I^0 ($\propto \sigma_I^0$) are reference subthreshold inert strengths to be defined later in this subsection. Again, we write separable crack-size functions for the shear component

$$f^S_A(c/a,\beta) = (c/a)^{1/2}(\{1-[1-(\beta a/c)^2]^{1/2}\} - [\nu/(2-\nu)]\{1-[1-(\beta a/c)^2]^{3/2}\}) \qquad c \geqslant \beta a \qquad (15)$$

and the tensile component

$$f^T_A(c/a,\beta) = (c/a)^{1/2}[1-(\beta a/c)^2]^{1/2} \qquad c \geqslant \beta a \qquad (16)$$

in analogy to Equations 8 and 9. Plots of these crack-size functions are included in Fig. 6.

The total stress-intensity factor for superposed residual and applied mode I and II fields is therefore [36]

$$K = [(K^I_R + K^I_A)^2 + (K^{II}_R + K^{II}_A)^2]^{1/2} \qquad (17)$$

With the equality

$$\sigma_A/\sigma_I^0 = \tau_A/\tau_I^0 \qquad (18)$$

Equation 17 becomes

$$\begin{aligned} K(c,a,\beta,\sigma_A) = Ha^{1/2}\{&[\alpha^T_R f^T_R(c/a,\beta) \\ &+ (\sigma_A/\sigma_I^0)\alpha^T_A f^T_A(c/a,\beta)]^2 \\ &+ [\alpha^S_R f^S_R(c/a,\beta) \\ &+ (\sigma_A/\sigma_I^0)\alpha^S_A f^S_A(c/a,\beta)]^2\}^{1/2} \end{aligned} \qquad (19)$$

Plots of $K(c/a)/Ha^{1/2}$ are shown at different applied stress levels σ_A in Fig. 8. Note the advent of a second unstable branch, 3, with a corresponding equilibrium point $c = c_3$ at $K = T_0$. Three possible fault instability configurations are represented.

(a) *Postthreshold strength*, Fig. 8a. In this case the initial shear fault configuration is postcritical; $a > a^*$, the crack pops in from unstable branch 1 to stable branch 2 before application of the external tensile load, i.e. at $\sigma_A = 0$. Subsequent loading, $\sigma_A > 0$, then causes the crack at c_2 to grow stably in equilibrium at $K(c_2) = K_C = T_0$

$$\begin{aligned} K(c,a,\beta,\sigma_A) = Ha^{1/2}\{&[\alpha^T_R f^T_R(c/a,\beta) \\ &+ (\sigma_A/\sigma_I^0)\alpha^T_A f^T_A(c/a,\beta)]^2 \\ &+ [\alpha^S_R f^S_R(c/a,\beta) + (\sigma_A/\sigma_I^0) \\ &\times \alpha^S_A f^S_R(c/a,\beta)]^2\}^{1/2} = T_0 \end{aligned} \qquad (20)$$

At $\sigma_A = \sigma_M$, $c = c_2 = c_3 = c_M$, as determined by the condition $\mathrm{d}K(c)/\mathrm{d}c = 0$, $\mathrm{d}^2K/\mathrm{d}c^2 > 0$, the system becomes unconditionally unstable. Failure is then said to be *propagation-controlled.*

We may note from Fig. 6 that it is the tensile components, i.e. the terms in f^T_A and f^T_R, that control this critical condition. Inserting $c \gg a$ in Equations 9 and 16, and recalling Equation 18, the instability requirement in Equation 19 yields

$$c_M = (3\alpha^T_R \sigma_I^0/\sigma_A \alpha^T_A)^{1/2} a \qquad (21a)$$

$$\sigma_M = \sigma_I^0[3(T_0/4H)^{4/3}/\alpha_R^{T1/3}\alpha^T_A]/a^{2/3} \qquad (21b)$$

These are of essentially the same limiting form as the equations derived previously [19] for postthreshold indentation cracks. Although not exact, they serve as a useful first approximation for later data analysis.

(b) *Subthreshold strength, activated failure*, Fig. 8b. The initial shear fault configuration is subcritical, i.e. $a < a^*$; but only just, such that, when the crack is induced to pop-in from c_I at intermediate applied stress σ_A, it arrests at $c = c_2$ on branch 2. Further loading to $\sigma_A = \sigma_M$ is then required to grow the crack at $K(c_2) = T_0$ to c_M, in which case the strength is given by the propagation-controlled formulation described in case (a).

(c) *Subthreshold strength, spontaneous failure*, Fig. 8c. The initial shear fault configuration is again subcritical, but at $a \ll a^*$. When the system at $c = c_I$ becomes unstable at critical stress $\sigma_A = \sigma_I$ the minimum between branches 2 and 3 lies either above the $K = T_0$ line or disappears altogether, so that extension is unlimited

$$K(c_I, a, \beta, \sigma_I) = Ha^{1/2}\{[\alpha_R^T f_R^T(c_I/a, \beta) + (\sigma_I/\sigma_I^0)\alpha_A^T f_A^T(c_I/a, \beta)]^2 + [\alpha_R^S f_R^S(c_I/a, \beta) + (\sigma_I/\sigma_I^0)\alpha_A^S f_A^S(c_I/a, \beta)]^2\}^{1/2} = T_0 \quad (22)$$

The failure is now *initiation-controlled.*

The subthreshold strength σ_I may now be determined as a function of indentation size a by direct inversion of Equation 22 to obtain $\sigma_I(a)$. From Fig. 6 we see that it is the shear components f_A^S and f_R^S that control the strength in this region.

A functional plot of the critical applied stress against indentation size a, or alternatively against load P from Equation 1 is presented in schematic form in Fig. 9. From the above description it is clear that the strength at any given value of a will be determined by whichever of σ_M and σ_I is the higher, as indicated by the composite solid curve. Thus the postthreshold, propagation-controlled strength region, where Equation 20 has its instability, lies to the right of the point (σ_M^*, a^*). Similarly, the initiation-controlled, spontaneous subthreshold strength region defined by Equation 22 lies to the left of the point (σ_I^0, a^0). This point defines the reference quantity σ_I^0 introduced earlier in Equation 14. The activated subthreshold region, where the radial crack pops in *en route* to propagation-controlled failure, falls within the intervening range $a^0 < a < a^*$.

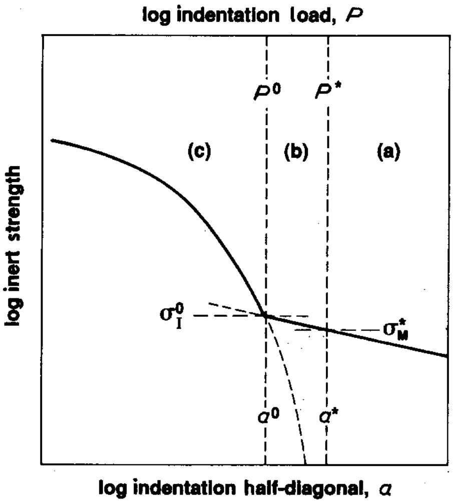

Figure 9 Schematic plot of inert strength σ against indentation size a, for the three regions (a), (b), (c) defined in Fig. 8. Points (σ_M^*, a^*) and (σ_I^0, a^0) delineate the three strength regions defined in Fig. 8.

4. Comparison of theory and experiment

Let us now fit the theory to existing data for crack initiation threshold and strength under inert testing conditions. These data are available for three silicate glasses: one normal, soda-lime; and two anomalous, fused silica and borosilicate (Table I).

4.1. Critical condition for radial crack pop-in

Consider first experimental data for radial crack pop-in from Vickers indentations in polished and annealed glasses, under the exclusive action of the residual contact stresses, in inert (dry nitrogen gas) environment [5, 7]. In normal (soda-lime) glass the pop-in event is well defined: below the critical indentation size there is no perceptible sign of radial crack extension outside the hardness impression ($c_I^* = \beta a + \Delta c, \Delta c \ll a$); above the critical size the radial cracks are clearly visible (typically, $c_2^* \approx 2$ to $3\ a$). In anomalous (fused silica and borosilicate) glasses the pop-in is much less pronounced ($c_2^* < 2a$), with relatively small radial crack dimensions.

The $K_R(c)$ curves in Figs 10 to 12 for the three glasses are fits of Equation 10 to these data. In these figures the full curves represent the fitted function at the critical indentation size a^* and pop-in crack dimension c_2^*, measured under environment-free conditions [26, 38, 39], for $\beta = 0.923$. The horizontal broken line on this plot indicates the literature value of $K_C = T_0$. To obtain the fits the parameters α_R^S and α_R^T are adjusted iteratively to satisfy two extreme requirements: that $K_R(c_I^*) = T_0$, i.e. the subsidiary minimum at c_I^* coincides with the horizontal broken line for equilibrium extension; and that $K_R(c_2^*) = T_0$, i.e. the pop-in length c_2^* corresponds to the measured

TABLE I Values of material parameters for silicate glasses used in this study. Data from [23].

	E (GPa)	H (GPa)	T_0 (MPa m$^{1/2}$)
Soda-lime	70	5.5	0.75
Fused silica	76	7.0	0.79
Borosilicate	64	6.1	0.76

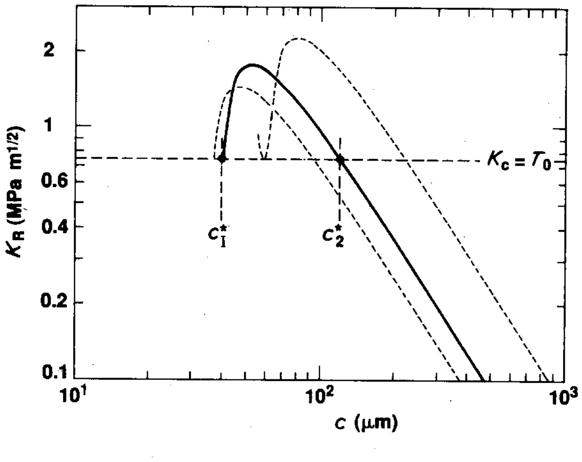

Figure 10 Plot of K_R (c) for soda-lime glass. Full curve is for $\beta = 0.923$, adjusted to correspond to critical indent size $a^* = 42.6$ μm ($P^* = 20.0$ N) [38] and pop-in length $c_2^* = 120$ μm [20]. Broken curves are for $\beta = 0.846$ (upper) and 1.0 (lower), corresponding to predicted scatter a* = 36.7 to 66.1 μm ($P^* = 14.8$ to 48.0 N).

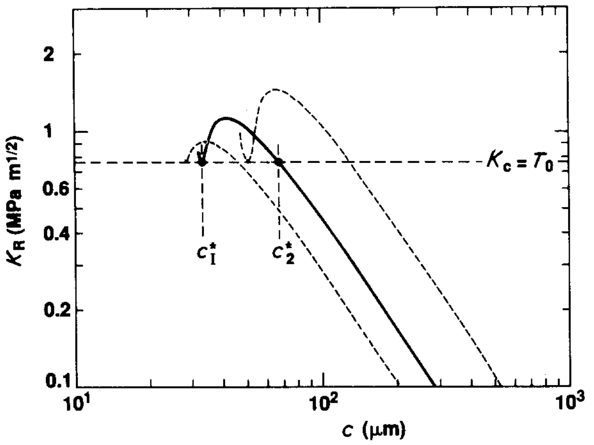

Figure 11 Same as Fig. 10, but for fused silica. Full curve is for critical indent size $a^* = 32.7$ μm ($P^* = 15.0$ N) [38] and pop-in length $c_2^* = 59.0$ μm [8]. Broken curves correspond to predicted scatter $a^* = 26.0$ to 52.0 μm ($P^* = 9.5$ to 37.9 N).

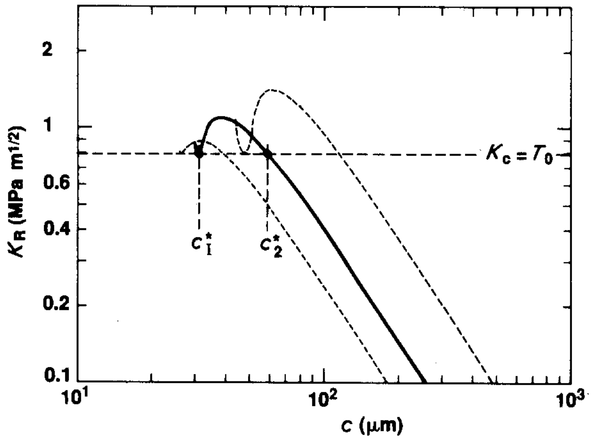

Figure 12 Same as Fig. 10, but for borosilicate glass. Full curve is for critical indent size $a^* = 35.1$ μm ($P^* = 15.0$ N) and pop-in length $c_2^* = 67.5$ μm [8, 22]. Broken curves correspond to predicted scatter $a^* = 28.3$ to 55.6 μm ($P^* = 9.7$ to 37.7 N).

TABLE II Values of adjustable α coefficients and reference strength σ_I^0 from data fits for three silicate glasses studied.

	α_R^T	α_R^S	α_A^T	α_A^S	σ_I^0 (MPa)
Soda-lime	0.0984	0.0072	0.0067	0.0235	56.5
Fused silica	0.0524	0.0073	0.0084	0.0252	95.3
Borosilicate	0.0606	0.0077	0.0107	0.0259	111.7

value. (In making these adjustments it is useful to recall that starting values of the α terms in the iteration may be obtained from the first approximations $f_R^T(c_I^*/a, \beta) = 0, f_R^S(c_2^*/a, \beta) = 0$, alluded to in Section 3.2.) The comparative "strength" of the pop-in event in normal glasses is evident in the $K_R(c)$ plots. Values of the calibrated α parameters are shown in Table II.

Included as the dashed curves in Figs 10 to 12 are companion plots for $\beta = 0.846$ and 1.000, using the same α parameters but adjusting a^* to meet the requirements for pop-in. Such a plot gives an indication of the potential scatter in the critical indentation size and in the attendant radial crack pop-in length.

4.2. Inert strength

Now consider experimental inert strength data for the three silicate glasses, in both postthreshold and subthreshold regions [3, 8, 17, 22, 30]. The postthreshold data are from Vickers-indented rod specimens. Data from subthreshold indentations are taken on heavily etched and annealed rods and fibres, so as to eliminate competing natural flaws.

These strength data are plotted in Figs 13 to 15 as function of indentation size a or load P as mean and standard deviation points. The full curves are fits of the functions σ_M evaluated from Equation 20 and σ_I from Equation 22 for $\beta = 0.923$, using the calibrated parameters α_R^S and α_R^T from Section 4.1 and adjusting α_A^S and α_A^T along with σ_I^0. (Again, in making these adjustments it is useful to obtain first approximations, e.g. Equation 21b for α_A^T, before iterating.) Values of α_A^S, α_A^T and σ_I^0 are included in Table II. The general features of the earlier schematic Fig. 9 are evident in these fits.

Comparative plots of the inert strength function for $\beta = 0.846$ and 1.000 are included in Figs 13 to 15. The

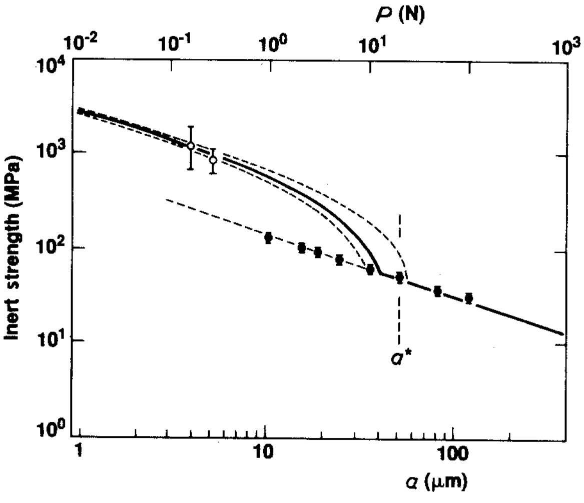

Figure 13 Inert strength plotted against indentation half-diagonal (lower axis) or contact load (upper axis) for soda-lime glass. Experimental data points are means and standard deviations [8, 22, 30]: postthreshold, closed symbols; subthreshold, open symbols. Curves are fits to theory, for $\beta = 0.923$ (full), and $\beta = 0.846$ and 1.000 (broken).

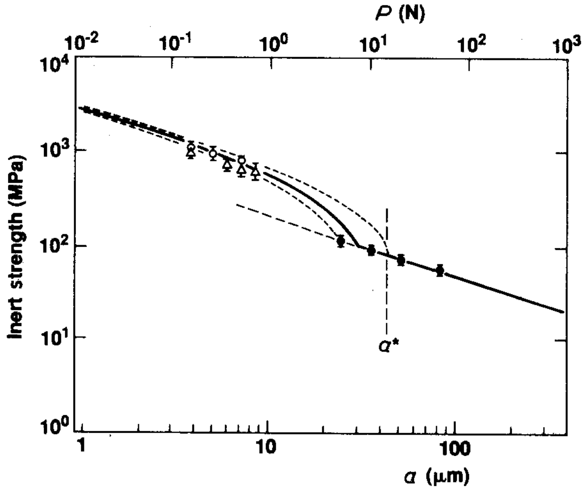

Figure 14 Same as Fig. 13, but for fused silica. Data from refs [6, 8] (circles) and [17] (triangles).

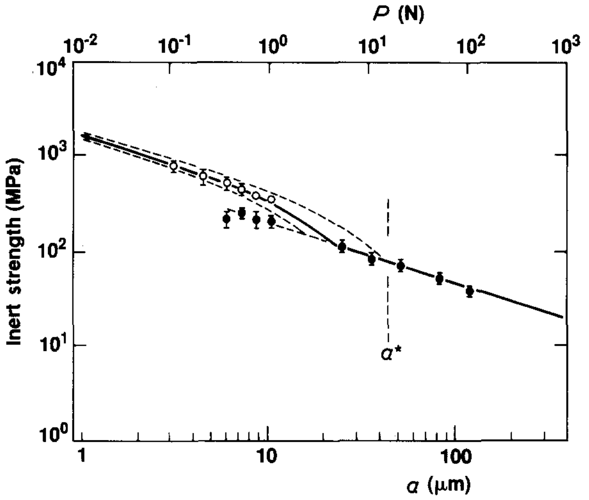

Figure 15 Same as Fig. 13, but for borosilicate glass. Data from [3, 22].

spread in the curves is substantially greater in the subthreshold than the postthreshold regions, reflecting the experimental standard deviation error bars, although the correspondence between experimental and predicted spreads is by no means exact.

Appropriate $K(c)$ functions in Equation 19 are generated for soda-lime glass in Fig. 16, for selected indentation sizes in the postthreshold, subthreshold-activated and subthreshold-spontaneous regions. The plots include curves at zero, intermediate and critical applied stress. These diagrams usefully indicate the evolution of the instability configurations in the different regions.

One point concerning the distinction between the inert strength regions delineated in Fig. 9 requires elaboration. Some of the postthreshold data in Figs 13 to 15 extend into the subthreshold domain at $a < a^0$. This reflects the experimental impracticality in maintaining strict equilibrium testing conditions throughout the complete indentation-strength testing sequence. In reality, trace amounts of moisture may cause radial cracks to pop-in after indentation but before strength testing, with increasingly smaller delay time the closer one approaches the critical indentation size a^* (delayed pop-in, see Part II). Indeed, for this reason it is difficult to get subthreshold strength data at all for values of a close to a^0. Accordingly, those points along the extended postthreshold curve are not representative of a truly inert-environment history, and are therefore included in the (extrapolated) postthreshold rather than the subthreshold curve fits.

5. Discussion

We have outlined a fracture mechanics model that allows a semi-quantitative analysis of the more important elements of mechanical behaviour of glasses with indentation flaws, namely the critical conditions for radial crack pop-in and the strength in the subthreshold region. Thus far we have considered only inert testing conditions, although, as we shall see in Part II, our formulation is readily adaptable to kinetic, environment-sensitive conditions. In deriving this model we have preserved the crux of earlier continuum-based treatments of postthreshold indentation cracks, yet have built an essential element of discreteness into the subthreshold micromechanics by assuming the radial cracks to generate from shear faults within the contact zone. In this way we have developed a universal formalism which tends asymptotically in limiting cases of very small and very large cracks to previously well defined relations for crack propagation and initiation.

As indicated in Sections 2 and 3, the residual stress term is crucial in the micromechanics of crack initiation. In our model the component of the near-field residual stress that primarily determines the critical indentation size is that associated with frictional tractions over the shear-fault interface, i.e. the α_R^S term in Equation 10. This frictional element is missing from earlier models of crack initiation [13, 14, 16]. The pop-in length, on the other hand, is primarily determined by the tensile component arising from elastic–plastic mismatch stresses, the α_R^T term in Equation 10. It is the far-field asymptotic form of this component that is considered in most treatments of crack propagation. We reemphasize that the root cause of the initiation threshold, as expressed by Equation 11, lies in the scaling of the K_R-field with the fault dimension (a) and not the stress intensity (H) in Equations 10 and 19 [13–15, 28].

Perhaps the most important result of the model is its capacity to account for the different inert-strength responses in the postthreshold and subthreshold regions. The subthreshold strengths are higher than one would expect from simple extrapolation of postthreshold data because, at low indentation sizes (in the spontaneous failure region $a < a^0$), the applied stress to *initiate* a radial crack exceeds the stress to *propagate* that crack to instability, i.e. $\sigma_I > \sigma_M$ in Fig. 9. The model also explains, at least in part, why the scatter in strengths is dramatically higher in the subthreshold than in the postthreshold region: namely the extreme sensitivity of the K_R-field to the fault location in the inhomogeneous near-contact stress field at very small crack sizes. Our analysis thus offers a self-consistent description of the transition from postthreshold to subthreshold strength regions as the indentations are reduced in size below the critical value.

An alternative graphical scheme for distinguishing the different regions of strength behaviour is to transpose Equation 19 and solve directly for the function $\sigma_A(c)$ at equilibrium, $K = K_C = T_0$. We plot the resulting function at indentation sizes $a_1 < a_2 < a_3 < a_4 < a_5$ for soda-lime glass in Fig. 17. Instabilities are indicated by arrows in the diagram. The strength in each of these curves is determined by the principal maximum. Postthreshold failure configurations are apparent at the higher values of a, subthreshold at the lower values (cf. Fig. 16): $a_5 > a^*$ ($P_5 > P^*$), the radial cracks pop-in spontaneously at $\sigma_A = 0$, and thereafter grow up the second stable branch of the $\sigma_A(c)$ curve to instability at $\sigma_A = \sigma_M$; $a_4 = a^*$ ($P_4 = P^*$), the indentation is at threshold, so

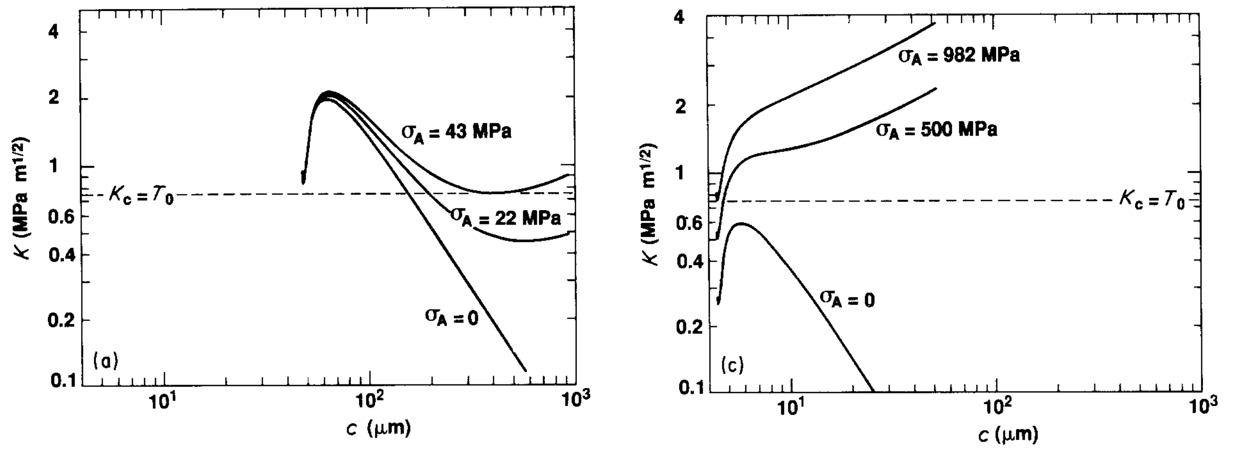

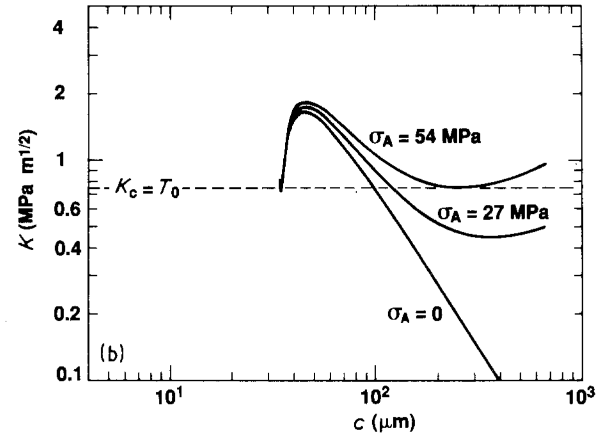

Figure 16 Plots of $K(c)$ in Equation 19 for soda-lime glass, for three regions: (a) postthreshold, $a = 52.2$ μm ($P = 30.0$ N), $\sigma_M = 43$ MPa; (b) subthreshold activated, $a = 36.9$ μm ($P = 15.0$ N), $\sigma_M = 54$ MPa; (c) subthreshold spontaneous, $a = 4.8$ μm ($P = 0.25$ N), $\sigma_I = 982$ MPa. (cf. Fig. 8.)

that the first maximum is at $\sigma_A = 0$, whence an infinitesimal applied stress is sufficient to cause pop-in to the second stable branch, leading to $\sigma_A = \sigma_M$ as previously; $a_3 = a^0 < a^*$ ($P_3 = P^0 < P^*$), the conditions for pop-in over the first maximum and propagation over the second maximum coincide, and the strength is $\sigma_A = \sigma_M = \sigma_I = \sigma_I^0$; $a_2 < a^0$ ($P_2 < P^0$), the cracks become unstable at $\sigma_A = \sigma_I > \sigma_I^0$, and proceed to failure without "recognizing" the second maximum; $a_1 \ll a^0$ ($P_1 \ll P^0$), the initiation instability is even more pronounced, and the strength is again determined by $\sigma_A = \sigma_I$.

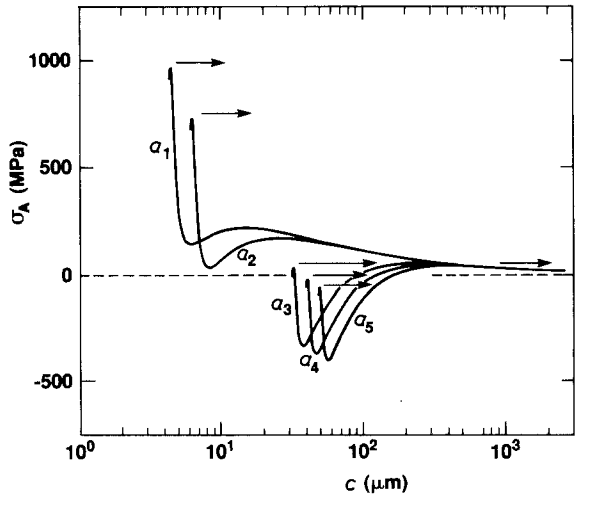

Figure 17 Plot of stress σ_A for equilibrium crack extension as a function of crack length c in soda-lime glass for five values of a, $\beta = 0.923$: $a_1 = 4.8$ μm ($P_1 = 0.25$ N); $a_2 = 6.7$ μm ($P_2 = 0.50$ N); $a_3 = a^0 = 34.4$ μm ($P_3 = P^0 = 13.0$ N); $a_4 = a^* = 42.6$ μm ($P_4 = P^* = 20.0$ N); $a_5 = 52.2$ μm ($P_5 = 30.0$ N). Arrows indicate instabilities.

The reader will note that to obtain the theoretical fits we have had to adjust four parameters in the K-field relations, the α terms. Many geometrical uncertainties in the analysis are implicit in these terms. For instance, the shear fault and the ensuing radial crack have been assumed to have a somewhat idealized penny-like geometry. Then, in using planar crack formulae to calculate stress-intensity factors we have ignored the fact that the radial crack extends at an abrupt angle from the edge of the shear fault, inevitably with mode III as well as mode II components along the extending front. With our simplistic fault-cavity representation of the contact field, we have assumed somewhat questionable spatial stress distribution functions (Fig. 4). In this context, the "agreement" between experimental data and theoretical fit can hardly be taken as proof of validity of the model: for that we must rely on the micrographic evidence described in Section 2.1. The model does, nevertheless, describe all the essential characteristics of the critical pop-in and ensuing strength phenomena, subthreshold and postthreshold, associated with indentation flaws.

Notwithstanding these qualifying remarks, it is interesting to compare quantitative features of the critical K_R-field plots in Figs 10 to 12 for the three glasses. The pop-in lengths are seen to be relatively small for the fused silica and borosilicate, reflecting lower values of α_R^T in Table II. This is consistent with the fact that fused silica and borosilicate are anomalous, with correspondingly smaller residual stress intensities, as pointed out in Section 2. With due allowance for quantitative variations of this kind in the *residual* field, the theory describes the inert strength characteristics for all three glasses in the subsequent *applied* field, Figs 13 to 15. There is therefore an implied generality in the analysis, so that extension to any other highly brittle material which exhibits the same kind of shear-fault–radial-crack process, e.g. quartz [7] and sapphire [12], may be envisaged; in such *crystallographic* materials, however, anisotropy in the deformation and fracture responses could have a profound influence on the fault-microcrack configuration that governs the initiation.

The formulation with its calibrated α parameters is now well placed to deal with another important aspect of crack pop-in and strength behaviour, that due to rate-dependent growth in an interactive chemical environment. We have already noted in Figs 13 to 15 one virtually unavoidable consequence of such slow crack growth, namely the tendency for the strengths of specimens exposed to moist environment in the interval between indentation and strength testing to undergo a premature degradation from subthreshold to postthreshold levels for flaws close to the critical contact size. This transition reflects the diminishing energy barrier to crack pop-in as the indentation size increases toward the critical value a^*, e.g. as one approaches a_4 in Fig. 17. From an engineering design standpoint, such a premature loss in strength could be highly dangerous. We shall explore the role of slow crack growth in detail in Part II.

6. Conclusions

The conclusions are as follows.

(1) A shear-fault–microcrack model of crack initiation and propagation for equilibrium indentation fracture conditions has been constructed.

(2) K-field expressions for the system have been derived by treating the deformation fault within the contact zone as a penny-like frictional shear crack with subsequent radial extension in residual and applied tensile stress fields outside the contact zone.

(3) Limiting forms of the equilibrium K-field equations reduce to results from earlier indentation fracture studies: for the residual stresses, in the near field to the critical contact size (or load) for initiation and in the far field to the familiar $P/c^{3/2}$ relation for propagation; for the far-field applied stresses to previous post-threshold inert-strength relations.

(4) The theory has been fitted to data for the critical indentation size for radial crack pop-in, and for corresponding strengths in the subthreshold and post-threshold domains, for soda-lime, fused silica and borosilicate glasses in inert environments.

(5) The fits in (4) have been used to "calibrate" adjustable parameters in the K-field relations, for application in Part II.

Acknowledgements

The authors are grateful to S. R. Choi, K. Jakus and J. E. Ritter for permission to reproduce data from their laboratory, to T-J. Chuang for determining the solution in Equation 12, to S. Line for assistance with the computations, and to R. F. Cook for discussions. This work was supported by a grant from E. I. Du Pont de Nemours and Co. and the U.S. office of naval Research.

References

1. R. OLSHANSKY and R. D. MAURER, *J. Appl. Phys.* **47** (1976) 4497.
2. D. KALISH and B. K. TARIYAL, *J. Amer Ceram. Soc.* **61** (1978) 518.
3. T. P. DABBS, D. B. MARSHALL and B. R. LAWN, *ibid.* **63** (1980) 224.
4. T. P. DABBS and B. R. LAWN, *Phys. Chem. Glasses* **23** (1982) 93.
5. B. R. LAWN, T. P. DABBS and C. J. FAIRBANKS, *J. Mater. Sci.* **18** (1983) 2785.
6. T. P. DABBS, C. J. FAIRBANKS and B. R. LAWN, ASTM STP 844, (American Society for Testing and Material Philadelphia, 1984) p. 142.
7. H. MULTHOPP, B. R. LAWN and T. P. DABBS, "Deformation of Ceramic Materials II", edited by R. E. Tressler and R. C. Bradt (Plenum, New York, 1984) p. 681.
8. T. P. DABBS and B. R. LAWN, *J. Amer. Ceram. Soc.* **68** (1985) 563.
9. B. R. LAWN, D. B. MARSHALL and T. P. DABBS, *Strength of Glass*, edited by C. R. Kurkjian (Plenum, New York, 1985) p. 249.
10. J. T. HAGAN, *J. Mater. Sci.* **14** (1979) 2975.
11. *Idem., ibid.* **15** (1980) 1417.
12. H. M. CHAN and B. R. LAWN, *J. Amer. Ceram. Soc.* **71** (1988) 29.
13. B. R. LAWN and A. G. EVANS, *J. Mater. Sci.* **12** (1977) 2195.
14. K. E. PUTTICK, *J. Phys. D* **11** (1978) 595.
15. B. R. LAWN and D. B. MARSHALL, *J. Amer. Ceram. Soc.* **62** (1979) 347.
16. S. S. CHIANG, D. B. MARSHALL and A. G. EVANS, *J. Appl. Phys.* **53** (1982) 312.
17. K. JAKUS, J. E. RITTER, S. R. CHOI, T. LARDNER and B. R. LAWN, *J. Non-Cryst. Solids* **102** (1988) 82.
18. R. HILL, "The Mathematical Theory of Plasticity" (Oxford University Press, London, 1950) Ch. 5, eqn (8).
19. D. B. MARSHALL and B. R. LAWN, *J. Mater. Sci.* **14** (1979) 2001.
20. B. R. LAWN, A. G. EVANS and D. B. MARSHALL, *J. Amer. Ceram. Soc.* **63** (1980) 574.
21 D. B. MARSHALL, B. R. LAWN and P. CHANTIKUL, *J. Mater. Sci.* **14** (1979) 2225.
22. T. P. DABBS, B. R. LAWN and P. L. KELLY, *Phys. Chem. Glasses* **23** (1982) 58.
23. A. ARORA, D. B. MARSHALL, B. R. LAWN and M. V. SWAIN, *J. Non-Cryst. Solids* **31** (1979) 415.
24. J. LANKFORD, *J. Mater. Sci.* **16** (1981) 1177.
25. B. R. LAWN and M. V. SWAIN, *J. Mater. Sci.* **10** (1975) 113.
26. D. B. MARSHALL, B. R. LAWN and A. G. EVANS, *J. Amer. Ceram. Soc.* **65** 561 (1982).
27. T. P. DABBS and B. R. LAWN, *ibid.* **65** (1982) C-37.
28. B. R. LAWN, T. JENSEN and A. ARORA, *J. Mater. Sci.* **11** (1976) 573.
29. B. R. LAWN and T. R. WILSHAW, *ibid.* **10** (1975) 1049.
30. D. B. MARSHALL and B. R. LAWN, *J. Amer. Ceram. Soc.* **63** (1980) 532.
31. P. CHANTIKUL, B. R. LAWN and D. B. MARSHALL, *ibid.* **64** (1981) 322.
32. B. R. LAWN, D. B. MARSHALL, G. R. ANSTIS and T. P. DABBS, *J. Mater. Sci.* **16** (1981) 2846.
33. G. I. BARENBLATT, *Adv. Appl. Mech.* **7** (1962) 55.
34. Y-W. MAI and B. R. LAWN, *Ann. Rev. Mater. Sci.* **16** (1986) 415.
35. G.C. SIH, "Handbook of Stress Intensity Factors" (Lehigh University Press, Bethlehem, Pa., 1973).
36. B. R. LAWN and T. R. WILSHAW, "Fracture of Brittle Solids" (Cambridge University Press, London, 1975).
37. T. J. CHUANG, personal communication.
38. C. J. FAIRBANKS, unpublished work.
39. T. P. DABBS, PhD Thesis, University of New South Wales, Australia (1984)

Received 17 October 1989
and accepted 20 March 1990